Supporting Information for

Global Estimates and Long-Term Trends of Fine Particulate Matter Concentrations (1998-2018)

Melanie S. Hammer[1,2]*, Aaron van Donkelaar[2,1], Chi Li[2,3], Alexei Lyapustin[4,5], Andrew M. Sayer[4,5], N. Christina Hsu[4], Robert C. Levy[4], Michael J. Garay[6], Olga V. Kalashnikova[6], Ralph A. Kahn[4], Michael Brauer[7,8], Joshua S. Apte[9], Daven K. Henze[10], Li Zhang[11,12], Qiang Zhang[13,14], Bonne Ford[15], Jeffrey R. Pierce[15], Randall V. Martin[1,2,16]

Correspondence: melanie.hammer@wustl.edu

[1]Department of Energy, Environmental & Chemical Engineering, Washington University in St. Louis, St. Louis, Missouri, United States

[2]Dept. of Physics and Atmospheric Science, Dalhousie University, Halifax, N.S. Canada

[3]Department of Chemistry, University of California, Berkeley, Berkeley, CA, USA.

[4]Earth Sciences Division, NASA Goddard Space Flight Center, Greenbelt, Maryland, USA

[5]Goddard Earth Sciences Technology and Research, Universities Space Research Association, Greenbelt, Maryland, USA

[6]Jet Propulsion Laboratory, California Institute of Technology, Pasadena, California

[7]School of Population and Public Health, The University of British Columbia, 2206 East Mall, Vancouver, British Columbia V6T1Z3, Canada

[8]Institute for Health Metrics and Evaluation, University of Washington, Seattle USA

[9]Department of Civil, Architectural and Environmental Engineering, University of Texas at Austin, Austin, TX USA 78712

[10]Department of Mechanical Engineering, University of Colorado Boulder, Boulder, Colorado, USA.

[11]CIRES, University of Colorado, Boulder, CO, USA

[12]Global Systems Division, Earth System Research Laboratory, NOAA, Boulder, CO, USA

[13]Ministry of Education Key Laboratory for Earth System Modeling, Department of Earth System Science, Tsinghua University, Beijing, China

[14]Collaborative Innovation Center for Regional Environmental Quality, Beijing, China

[15]Department of Atmospheric Science, Colorado State University, Fort Collins, USA

[16]Harvard-Smithsonian Center for Astrophysics, Cambridge, Massachusetts, USA

*corresponding author: Melanie S. Hammer, Department of Energy, Environmental & Chemical Engineering, Washington University in St. Louis, St. Louis, Missouri, United States, melanie.hammer@wustl.edu

This Supporting Information includes 3 sections of text, 5 tables, and 3 figures on 23 pages, including this cover sheet.

1. Description of Satellite AOD Sources

We use AOD retrieved from radiances measured by four satellite instruments: twin MODerate resolution Imaging Spectroradiometer (MODIS) instruments, the Multi-angle Imaging Spectroradiometer (MISR) instrument, and the Sea-viewing Wide Field-of-view Sensor (SeaWiFS) instruments. A summary of the satellite AOD sources used is given in Table S1a.

The twin MODIS instruments have flown on the Terra and Aqua satellites since 2000 and 2002, respectively. Terra has a descending orbit, passing the equator at 10:30 local time, while Aqua has an ascending orbit, passing equator at 13:30 local time. Both MODIS instruments have a wide spectral range of 0.41 μm to 14.5 μm and a broad swath width of 2330 km which allows for nearly global daily coverage.[1] We use AOD retrieved from three retrieval algorithms that process MODIS measured radiances: Dark Target (DT), Deep Blue (DB), and the Multi-Angle Implementation of Atmospheric Correction (MAIAC).

The DT retrieval algorithm[2] performs a simultaneous inversion of two visible (0.47 μm and 0.66 μm) and one shortwave-IR (2.12 μm) channel to retrieve AOD over dark surfaces (i.e. vegetated land surfaces and dark soils). DT also retrieves AOD over ocean, but we are not using those data here. The DB retrieval algorithm[3] uses blue wavelength measurements where the surface reflectance over land tends to be much lower than at longer wavelengths, allowing for the retrieval of aerosol properties over both bright and dark surfaces. This is especially true over desert surfaces. Both MODIS DT and DB are reported at a wavelength of 550 nm and a nominal spatial resolution of 10 km at nadir. We use the recently reprocessed MODIS collection 6.1 (C6.1) products which employ (1) an updated radiometric calibration that improves instrument stability over time, (2) updates to the surface reflectance treatment used in the DT algorithm,[4] (3) improvement to the

surface modelling in elevated terrain, (4) reduction in artifacts in heterogeneous terrain, and (5) improved internal smoke detection masks used in the DB algorithm.[3,5]

The MAIAC algorithm[6] retrieves aerosol information at 470 nm over both bright and dark land surfaces simultaneously with surface bidirectional reflectance using time-series analysis of MODIS L1B radiance measurements for up to 16 days. With removal of the long-term calibration trends and cross-calibration of MODIS Terra to MODIS Aqua in Collection 6,[7] MAIAC processes the two sensors jointly, which creates significantly increased observation frequency required for accurate surface characterization. MAIAC was officially released in May 2018, providing AOD at a fine spatial resolution of 1 km globally over the land and coastal ocean for the entire MODIS record. However, this work started earlier and used an internally released MAIAC dataset that lacked parts of Canada, eastern Siberia, and the Indo-Pacific region (e.g., Indonesia, Oceania, Australia, New Zealand).

The SeaWiFS instrument flew on SeaStar, which had a noon overpass time, and was operational between 1997-2010. SeaWiFS maintained a highly accurate and stable calibration over its lifetime.[8] SeaWiFS provided measurements in eight spectral bands between 402-885 nm and had a 1500 km swath width that provided nearly daily global coverage. We used the version 4 SeaWiFS Deep Blue[8,9] data set that offers AOD at a wavelength of 550 nm with a horizontal pixel size of 13.5 km at nadir.

The MISR instrument is onboard the Terra satellite along with MODIS, and has been operational since 2000. MISR observes the earth at nine different viewing angles and four spectral bands (446, 558, 672, and 866 nm), with a swath width of 380 km all view angles that provides global coverage about once per week, every nine days at the equator, up to every two days near the poles.[10] The MISR retrieval algorithm uses the same-scene multi-angular views provided by the nine view-

angles to solve for surface and top-of-atmosphere reflectance contributions, providing AOD retrievals over bright and dark land surfaces without absolute surface reflectance assumptions.[11] We use AOD retrieved at 550 nm from the recently released MISR v23 algorithm,[12,13] which provides AOD at a spatial resolution of 4.4 km, which is a significant improvement over the 17.6 km resolution in the previous version of MISR AOD, along with better cloud screening and pixel-level uncertainty estimates.[12]

2. Description of the GEOS-Chem simulation

We use v11-01 of the GEOS-Chem chemical transport model (http://geos-chem.org) to simulate η, and as an additional AOD source. The simulation is driven by assimilated meteorological data from the recent MERRA-2 Reanalysis of the NASA Global Modeling and Assimilation Office (GMAO), which offers a consistent assimilation from 1979, including updates in both the Goddard Earth Observing System Model and the assimilation system.[14] Our simulation is conducted for the years 1998–2018 at a spatial resolution of $2° \times 2.5°$ with a nested resolution of $0.5° \times 0.625°$ over North America, Europe, and China, and 47 vertical levels. The top of lowest model layer is approximately 100 m. We follow the recommendations of Philip et al.[15] to use a chemical and transport operator duration of 20 min and 10 min, respectively. We include a non-local boundary layer mixing scheme.[16] We spin up the model for one month before each global and regional simulation to remove the effects of initial conditions.

GEOS-Chem contains a detailed oxidant-aerosol chemical mechanism.[17,18] The aerosol simulation includes the sulfate–nitrate–ammonium system,[18–20] primary carbonaceous aerosol,[21] sea salt,[22] and mineral dust[23] with an improved fine dust size distribution.[24] We include an anthropogenic fugitive, combustion, and industrial dust (AFCID) emissions inventory.[25] Semivolatile primary

organic carbon and secondary organic aerosol (SOA) formation[26] is included with updated SOA formation from isoprene via an irreversible up-take scheme.[27] HNO_3 concentrations are reduced to commensurate with prior work.[28] Relative humidity dependent aerosol optical properties are based on the Global Aerosol Data Set (GADS)[29,30] with updates for organics and secondary inorganics from aircraft observations,[31] mineral dust,[24,32,33] and for absorbing BrC.[34]

The anthropogenic emissions inventories in our simulation are summarized in Table S4. Global anthropogenic emissions are from the EDGAR v4.3.1 global inventory,[35] with speciated volatile organic compound (VOC) emissions from RETRO.[36] Emissions are over-written in areas with regional inventories, including the US (NEI11[37]), Canada (CAC; http://www.ec.gc.ca/pdb/cac/), Mexico (BRAVO[38]), Europe (EMEP; http://www.emep.int/), China (MEIC v1.2[39,40]), India (Lu et al.[41]) and elsewhere in Asia (MIX[39,40]). We doubled the Indian OC and BC emissions from Lu et al.[41] based on Philip et al.[42] and Fu et al.[43] Emissions from open fires for individual years from the GFED4 inventory[44] are included covering the years 1998-2018.

3. Algorithm for calculating combined $PM_{2.5}$ from satellites and simulation

Our algorithm to combine information from satellites and simulation follows van Donkelaar et al.,[45] with updates to ground-based AOD measurements, to the satellite AOD products, to the GEOS-Chem simulation, and to the resolution of our analysis.

The first step in the calculation of our combined $PM_{2.5}$ estimates is the common calibration of the separate AOD sources. Each source is translated onto a common 0.05° x 0.05° grid. For a consistent definition of uncertainty, we compare each AOD source with AERONET (Aerosol Robotic Network)[46] AOD at 550 nm. AERONET is a global sun photometer network that provides multi-wavelength AOD measurements with a high level of accuracy (the uncertainty associated with AERONET measurements is <0.02). We use level 2 of the version 3 AERONET data.[47]

There are different sources of error associated with satellite retrieved AOD than with simulated AOD, therefore their uncertainties need to be accounted for differently. For cloud-free and snow-free daytime scenes, one of the main sources of uncertainty associated with satellite retrieved AOD is the surface treatment used in the retrieval.[48] Therefore the daily satellite AOD retrievals are sampled to within 0.25° of each AERONET site and binned according to the Normalized Difference Vegetation Index (NDVI), which represents seasonally based changes in vegetation. Locally, calibrations are calculated at each AERONET site as the median slope and offset from reduced major axis linear regression of retrieved AOD with the AERONET values. The local calibrations are then expanded globally by calculating each pixel as the weighted average of all AERONET site-specific local calibrations, using inverse squared distance and the inverse of the Land Cover Similarity (LCS):

$$LCS_{i,j,k} = \sum_{n=1}^{N_{LT}} |LT_{i,j,n} - LT_{k,n}| \qquad [S1]$$

where $LT_{i,j,n}$ is the land cover type percentage of the pixel (i,j) for each land cover type (n) and $LT_{k,n}$ is the land cover type percentage of AERONET site (k) for each land cover type (n). The land cover type categories are defined by the MODIS land cover product.[49] The LCS allows similar mixtures of land cover to be weighted more strongly.

The residual uncertainty between the calibrated and observed AOD at each AERONET site is then calculated as the normalized root mean square difference:

$$NRMSD = \frac{\left(MEAN(AOD_{CALIBRATED} - AOD_{AERONET})^2\right)^{0.5}}{AOD_{AERONET}} \qquad [S2]$$

Local NRMSD are globally extended using inverse squared distance and LCS, following the approach used for the local calibration factors.

For the simulated AOD, to account for errors due to species-specific emissions and assumed aerosol microphysical properties, we calculate the relative uncertainty by applying the simulated fractional aerosol composition to each daily AERONET observation following van Donkelaar et al.[50] The local calibration factors are calculated as the absolute error of each species at each station as a function of magnitude. The local calibration factors are then extended globally using inverse distance squared and the cross-correlation weighted average of each AERONET site to each global pixel. The residual uncertainty is calculated as the component-specific NRMSD, and is extended globally using the inverse squared distance and cross correlation. The daily surface $PM_{2.5}$ concentrations from each source are obtained by applying the daily simulated AOD to $PM_{2.5}$ ratios (η). Evaluation of the simulation versus ground-based measurements indicates consistency with both AERONET AOD ($R^2=0.71$) and $PM_{2.5}$ monitors ($R^2=0.61$).

The daily AOD and $PM_{2.5}$ values are used to calculate monthly mean values. Missing AOD and $PM_{2.5}$ values within areas of more than 50% coverage are approximated using the interpolated ratio with the same data source during other years, or if necessary the interpolated ratio with simulated values during the same time period. Monthly AOD values from all N sources are combined using a weighted average, weighted by the product of the inverse residual AOD NRMSD, the inverse absolute percent difference between calibrated and uncalibrated AOD $\left(\frac{\Delta AOD_{adj}}{AOD}\right)$ and the local data density (N_{obs}) such that:

$$AOD = \frac{\sum_{n=1}^{N}\frac{1}{NRMSD_n} \times \left(\frac{\Delta AOD_{adj,n}}{AOD_n}\right)^{-1} \times N^2_{obs,n} \times AOD_n}{\sum_{n=1}^{N}\frac{1}{NRMSD_n} \times \left(\frac{\Delta AOD_{adj,n}}{AOD_n}\right)^{-1} \times N^2_{obs,n}} \qquad [S3]$$

$\Delta AOD_{adj,n}$ and AOD_n are set to a minimum of 0.01, and N_{obs} is set to a maximum of 5 observations per month for the purpose of weighting, even when more observations are included

in the calculation. The squaring of N_{obs} penalizes sparse observation density. Values exceeding 3 standard deviations of those within the surrounding 1° x 1° are replaced via linear interpolation. Figure S1 shows a scatter plot of the combined AOD data versus AOD measurements from AERONET. A high degree of consistency is apparent (R^2=0.84, slope=0.97).

The monthly $PM_{2.5}$ estimates are combined using similar weighting:

$$PM_{2.5} = \frac{\Sigma_{n=1}^{N}\frac{1}{NRMSD_n} \times \left(\frac{\Delta AOD_{adj,n}}{AOD_n}\right)^{-1} \times N_{obs,n}^2 \times PM_{2.5,n}}{\Sigma_{n=1}^{N}\frac{1}{NRMSD_n} \times \left(\frac{\Delta AOD_{adj,n}}{AOD_n}\right)^{-1} \times N_{obs,n}^2} \qquad [S4]$$

Spatial information from the 1 km MAIAC AOD retrieval is then incorporated by applying the climatology of its retrieved relative variation between 0.01° and 0.05°. Where MAIAC is unavailable, monthly AOD and $PM_{2.5}$ are linearly interpolated onto a 0.01° x 0.01° grid.

We use Geographically Weighted Regression (GWR) to predict and account for the bias in the annual mean of our geophysical $PM_{2.5}$ estimates ($GEO\ PM_{2.5}$). GWR is a statistical technique that allows the modelling of processes that vary over space.[51] GWR is an extension of least-squares regression that allows predictor coefficients to vary spatially by weighting the estimate-observation pairs at multiple geographic locations according to their inverse squared distance from individual observation sites.

We fit our GWR model coefficients at 1° x 1° intervals using $PM_{2.5}$ measured with ground-based monitors ($GM\ PM_{2.5}$) following the form:

$$\left(GM\ PM_{2.5} - \ GEO\ PM_{2.5}\right) = \beta_1 DST + \beta_2 SNAOC + \beta_3 ED \times DU \qquad [S5]$$

where

β_1 to β_3: represent spatially varying predictor coefficients,

ED: the log of the elevation difference between the local elevation and the mean elevation within the simulation grid cell according to the 1° x 1° ETOPO1 Global Relief Model (from the National Geophysical Data Center; http://www.ngdc.noaa.gov/mgg/global/seltopo.html),

DU: inverse distance to the nearest urban land surface based on the 1° resolution MODIS Land Cover Type Product (MCD12Q1),[49]

DST and *SNAOC*: compositional concentrations of mineral dust (*DST*) and the sum of sulfate, nitrate, ammonium, and organic carbon (*SNAOC*) are represented by the simulated relative contributions of each species applied to $GEO\,PM_{2.5}$ by weighting the near-surface aerosol concentration by the simulated compositional contribution of each species.[42]

We interpolate all predictors onto a common 0.01° grid. The GWR adds the most value where ground monitors are available, and the method will only improve as more ground monitors are added globally.

Table S1a: Summary of Satellite AOD Sources

Instrument	Satellite (Overpass Time)[a]	Retrieval Algorithm	Time Period Available	Time Period Used	Spatial Resolution	Temporal Resolution
MODIS	Terra (10:30)	C6.1 Dark Target C6.1 Deep Blue	2000-present			
				2002-2018[b]	10 km x 10 km	
	Aqua (13:30)	C6.1 Dark Target C6.1 Deep Blue	2002-present			Daily under viable conditions
	Terra/Aqua Combined	MAIAC	2000-present	2001-2018[c]	1 km x1 km	
MISR	Terra (10:30)	MISR v23	2000-present	2001-2018[d]	4.4 km x 4.4 km	Weekly under viable conditions
SeaWiFS	SeaStar (12:00)	Deep Blue version 4	1997-2010	1998-2010[e]	13.5 km x 13.5 km	Daily under viable conditions

a. Local time at the equator.

b. The years 2000-2001 were not yet available for the Terra MODIS C6.1 products at the time this project began.

c. The year 2000 was not yet available for MAIAC at the time this project began.

d. The year 2000 was not yet available for MISR v23 at the time this project began.

Table S1b: Summary of Other Data Sources

Data Source	Time Period Used	Spatial Resolution	Temporal Resolution	Usage
GEOS-Chem	1998-2018	$2° \times 2.5°$ (global) and $0.5° \times 0.625°$ over nested regions.	10 - 15 min (transport), hourly (chemistry and emissions)	AOD source, AOD to $PM_{2.5}$ relationship, speciated GWR predictors
AERONET version 3, Level 2	1998-2016[a]	Point observation	15 minutes under cloud- free conditions	AOD uncertainty assessment and calibration
MODIS Collection 5 Land Type Percentage (MCD12C1)	2001-2012	$1° \times 1°$ regridded onto global $0.01° \times 0.01°$ grid.	Annual	Global extension of AERONET- observed uncertainty, and GWR predictor (urban landcover)
ETOPO1 Global Relief Model	N/A	$1° \times 1°$ regridded onto global $0.01° \times 0.01°$ grid.	N/A	GWR predictor
$PM_{2.5}$ surface monitors	2010-2018	Point observation	Annual	Assessment and GWR calibration

a. The years 2017-2018 were not yet available for download from AERONET version 3 at the time this project began.

Table S2: Summary of anthropogenic emissions used in the GEOS-Chem simulation

Region	Inventory (Coverage)	Used Species	Annual Scale Factor[a]	Reference
World	EDGAR v4.3.1 (1970-2010)	CO, NO_x, SO_2, NH_3, OC, BC	N/A	Crippa et al.[35]
	RETRO (2000)	VOCs	from EDGAR v4.3.1, 1970-2010	Schultz et al.[36]
U.S.	EPA NEI11 (2011)	CO, NO_x, SO_2, NH_3, OC, BC, VOCs	NEI historical emission, 1990-2014	US Environmental Protection Agency[37]
Canada	CAC (2002-2008)	CO, NO_x, SO_2, NH_3, OC, BC	APEI, 1990-2014	Environment Canada[b]
Mexico	BRAVO (1999)	CO, NO_x, SO_2	from EDGAR v4.3.1, 1970-2010	Kuhns et al.[38]
Europe	EMEP (1990-2012)	CO, NO_x, SO_2, NH_3	N/A	Centre on Emissions Inventories and Projections[c]
China	MEIC v1.2 (2000-2015)	NO_x, SO_2, NH_3, OC, BC	N/A	Li et al.[39]
India	Lu et al.[41] (1998-2010)	SO_2, OC, BC	N/A	Lu et al.[41]
Asia	MIX (2008-2012)	CO, NO_x, SO_2, NH_3, OC, BC, VOCs	CO, NO_x, NH_3, VOCs, from EDGAR v4.3.1, 1970-2010, SO_2, OC, BC from Lu et al.[41]	Li et al.[39]

a. Annual scale factors are spatially resolved and applied only when the emission inventory lacks data for a certain year. Data in the closest available year is used if outside the available range.

b. http://www.ec.gc.ca/pdb/cac/

c. http://www.emep.int/

Table S3: The global number of direct $PM_{2.5}$ measurements available each year from the World Health Organization (WHO) Ambient (Outdoor) Air Quality Database.

Year	Number of measurements[a]
2010	1526
2011	1659
2012	1735
2013	1997
2014	2761
2015	3787
2016	4016
2017	3823
2018	2065

[a]Only sites with greater than 75% annual coverage were included.

Table S4: The coefficient of variation (R^2) and slope between the hybrid geophysical-statistical $PM_{2.5}$ estimates (at cross validated sites) and in-situ values for V4.GL.03 from this work and V4.GL.02 from van Donkelaar et al.[45] N is the number of comparison points.

Year	R^2		slope		N
	v.03	v.02	v.03	v.02	
2014	0.90	0.80	0.96	0.88	2761
2015	0.92	0.85	0.91	0.94	3783
2016	0.92	0.85	0.97	0.88	4016

Table S5: Population-weighted geophysical $PM_{2.5}$ trend (µg/m³/yr) for 1998-2018 with standard error in brackets, and population-weighted mean $PM_{2.5}$ (µg/m³) according to geophysical (GEO), GWR-adjusted hybrid (HBR), the Global Burden of Disease 2017 dataset (GBD)[52] and monitor for 2015, by Global Burden of Disease region. Population data are from the Gridded Population of the World database,[53] and unavailable years were obtained via linear interpolation.

| Region | Population [million people] | GEO $PM_{2.5}$ Trend | GEO $PM_{2.5}$ | HBR $PM_{2.5}$ | GBD $PM_{2.5}$ | At $PM_{2.5}$ Monitor Locations | | | | |
						GEO $PM_{2.5}$	HBR $PM_{2.5}$	GBD $PM_{2.5}$	Monitor $PM_{2.5}$	N [#]
Global	7345	0.04 (0.02)	41.8	46.9	55.7	40.8	43.2	50.8	44.9	3787
Asia Pacific, High Income	182	-0.09 (0.04)	18.8	18.9	16.9	32.1	32.7	25.2	23.3	24
Asia Central	86	-0.05 (0.03)	15.8	28.0	26.5	-	-	-	-	0
Asia East	1430	-0.04 (0.09)	49.7	48.6	57.6	51.1	53.4	63.8	55.9	1456
Asia South	1721	1.34 (0.19)	55.1	67.9	80.9	61.5	77.75	99.80	80.6	13
Asia, Southeast	648	0.004 (0.11)	29.3	26.7	22.6	-	-	-	-	0
Australasia	28	-0.03 (0.02)	2.7	4.8	8.3	2.8	5.4	6.9	7.4	35
Caribbean	39	-0.11 (0.05)	7.3	9.9	17.4	-	-	-	-	0
Europe, Central	115	-0.33 (0.05)	14.6	19.1	20.2	15.5	21.5	21.6	22.6	150
Europe, Eastern	209	-0.08 (0.06)	11.9	14.0	17.3	4.5	5.3	8.6	9.7	48
Europe, Western	423	-0.12 (0.02)	11.0	12.9	12.8	10.7	13.7	13.8	14.3	938
Latin America, Andean	57	-0.08 (0.08)	12.3	22.4	22.8	10.0	53.0	44.0	25.0	1
Latin America, Central	251	0.04 (0.06)	15.1	16.2	19.8	24.9	23.5	23.6	24.6	17
Latin America, Southern	64	-0.01 (0.02)	7.1	8.6	16.1	5.0	8.0	12.0	10.0	1
Latin America, Tropical	214	-0.03 (0.03)	9.1	10.1	13.5	-	-	-	-	0
North Africa/ Middle-East	488	0.09 (0.04)	22.7	29.1	55.8	43.2	57.6	63.0	72.0	4
North America, High Income	360	-0.06 (0.02)	9.0	8.5	7.8	8.9	8.5	8.0	8.6	1060
Oceania	10	0.05 (0.01)	5.9	5.4	12.0	2	2	12	8	1
Sub-Saharan Africa, Central	113	-0.12 (0.09)	30.0	32.6	42.4	-	-	-	-	0
Sub-Saharan Africa, East	416	0.06 (0.03)	17.3	21.1	36.4	-	-	-	-	0
Sub-Saharan Africa, Southern	78	0.04 (0.03)	11.2	11.9	25.2	-	-	-	-	0
Sub-Saharan Africa, West	391	-0.09 (0.12)	53.7	76.1	60.2	-	-	-	-	0

Table S6: Root Mean Square Error (RMSE) of GWR-adjusted hybrid PM$_{2.5}$ (HBR RMSE) and out-of-sample RMSE for the GWR-adjusted hybrid PM$_{2.5}$ (HBR_O RMSE) at monitor locations for 2015 by Global Burden of Disease region.

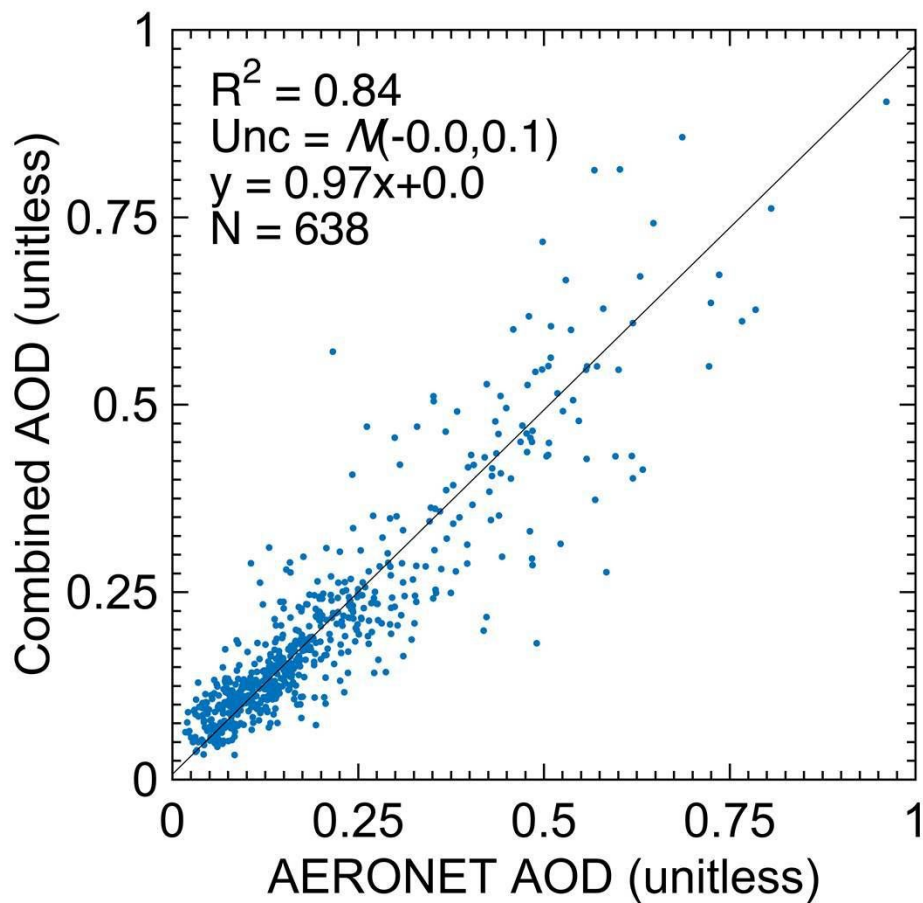| Region	At PM$_{2.5}$ Monitor Locations		
	HBR RMSE	HBR_O RMSE	N [#]
Global	6.89	6.80	3787
Asia Pacific, High Income	9.54	8.23	24
Asia Central	-	-	0
Asia East	10.06	10.14	1456
Asia South	15.62	17.26	13
Asia, Southeast	-	-	0
Australasia	1.76	1.98	35
Caribbean	-	-	0
Europe, Central	4.46	4.71	150
Europe, Eastern	3.30	3.61	48
Europe, Western	3.20	3.16	938
Latin America, Andean	27.98	-	1
Latin America, Central	5.26	5.61	17
Latin America, Southern	2.29	-	1
Latin America, Tropical	-	-	0
North Africa/ Middle-East	20.82	27.25	4
North America, High Income	1.78	1.85	1060
Oceania	6.34	-	1
Sub-Saharan Africa, Central	-	-	0
Sub-Saharan Africa, East	-	-	0
Sub-Saharan Africa, Southern	-	-	0
Sub-Saharan Africa, West	-	-	0

Figure S1: Scatter plot of the monthly mean combined AOD estimates versus monthly mean AERONET AOD for 2015. Only sites with measurements for at least 80% of the month and elevation less than 3000 m were included in the analysis. Included on the plots are the coefficient of variation (R^2), the normal distribution of uncertainty (N(bias,variance)), the line of best fit (y), and the number of comparison points (N).
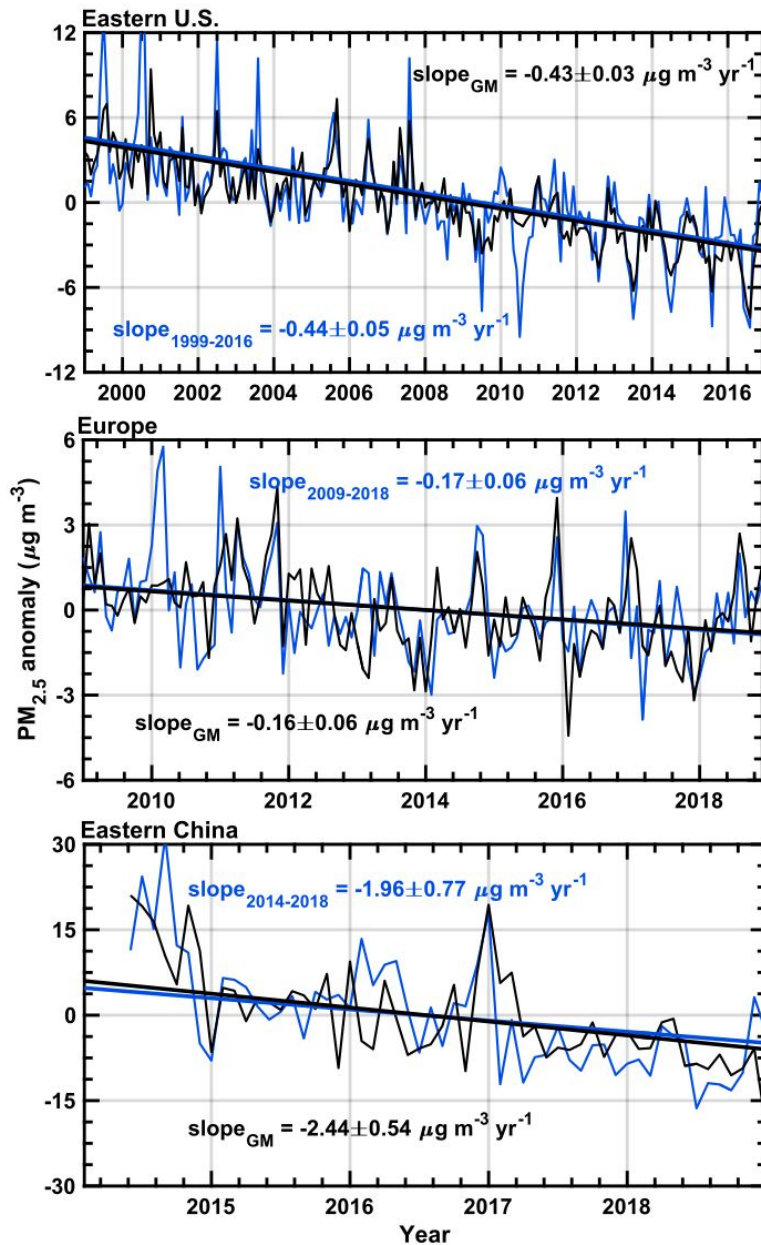
Figure S2: Regional monthly timeseries anomaly plots for population weighted mean geophysical $PM_{2.5}$ values coincidently sampled and evaluated with ground measurements. Blue lines and their corresponding linear fits (slope ± standard error) indicate geophysical $PM_{2.5}$ values, while black lines and their corresponding linear fits indicate regional ground measurements. Over the eastern U.S. (top panel) measurements are from the EPA for 1999-2016. Over Europe (middle-panel) measurements are from the European Environmental Agency for 2009-2018. Over eastern China (bottom panel) measurements are from China's national monitoring network for mid-2014-2018. Population estimates are from the Gridded Population of the World (GPW v4) database[87], and unavailable years were obtained via linear interpolation.
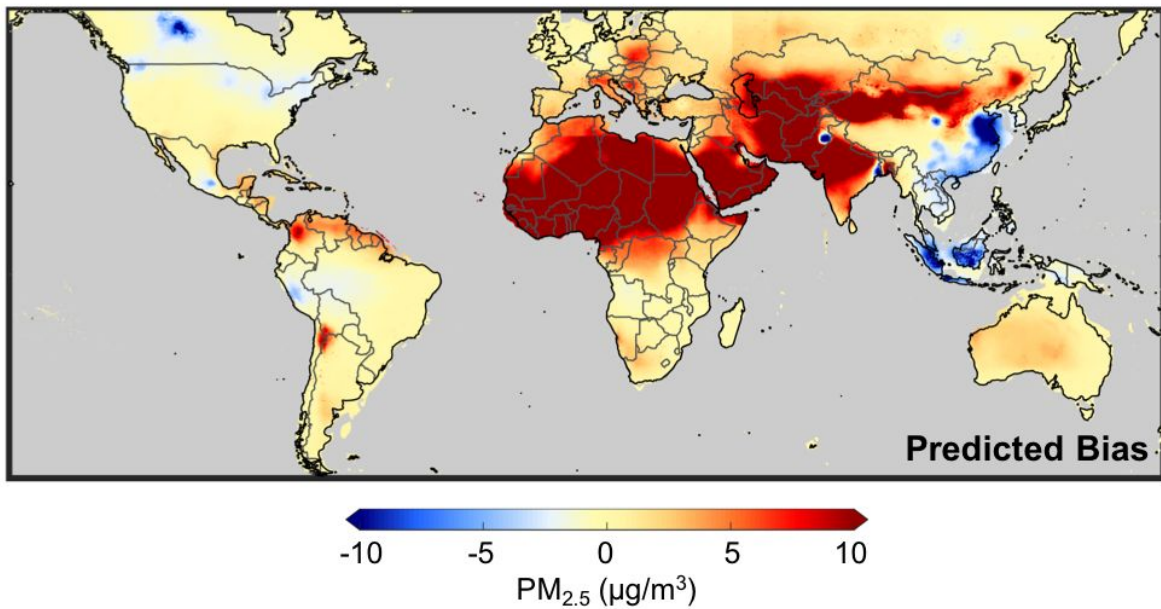
Figure S3: Bias predicted by geographically weighted regression between our geophysical PM$_{2.5}$ estimates (Figure 3) and in situ ground monitor data for 2015. Point locations correspond to individual monitors, with black dots representing direct PM$_{2.5}$ observations. Grey denotes water.
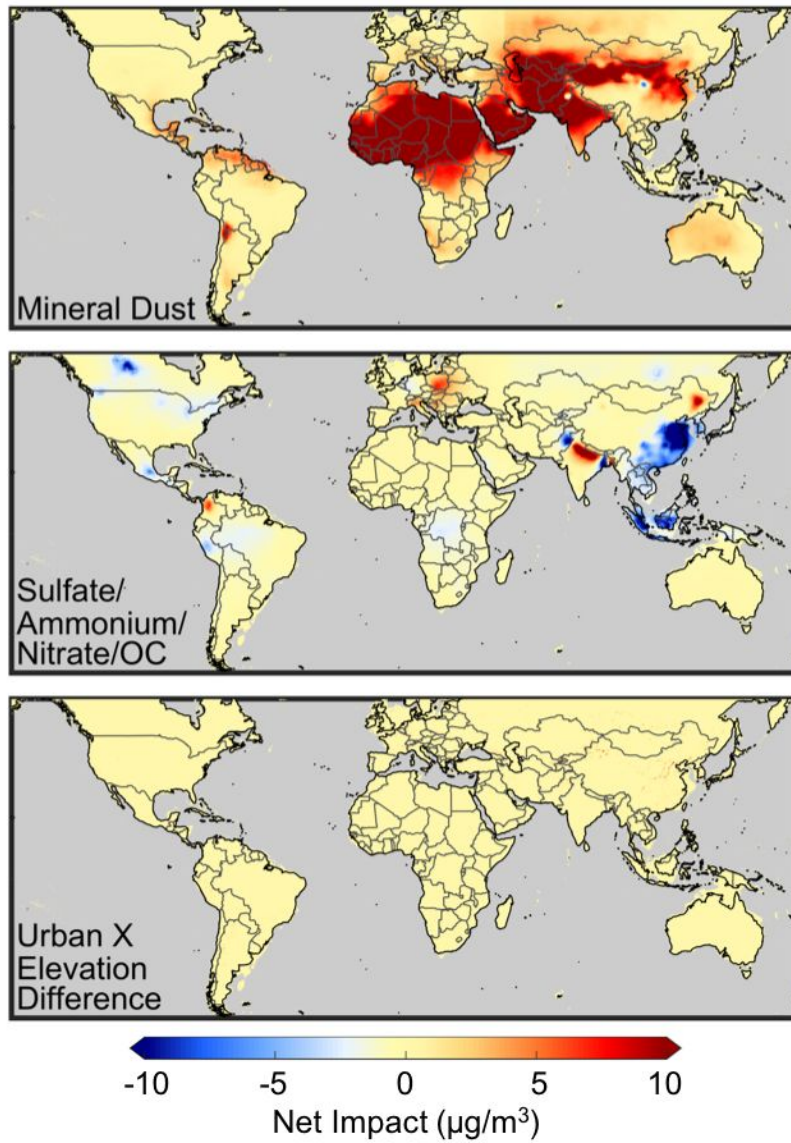
Figure S4: Net impact of individual predictors on the geographically weighted regression estimate of bias in geophysical PM$_{2.5}$ for 2015. Gray denotes water.

References

(1)   Sayer, A. M.; Munchak, L. A.; Hsu, N. C.; Levy, R. C.; Bettenhausen, C.; Jeong, M.-J. MODIS Collection 6 Aerosol Products: Comparison between Aqua's e-Deep Blue, Dark Target, and "Merged" Data Sets, and Usage Recommendations. *J. Geophys. Res. Atmos.* **2014**, *119* (24), 13,965-13,989. https://doi.org/10.1002/2014JD022453.

(2)   Levy, R. C.; Mattoo, S.; Munchak, L. A.; Remer, L. A.; Sayer, A. M.; Patadia, F.; Hsu, N. C. The Collection 6 MODIS Aerosol Products over Land and Ocean. *Atmos. Meas. Tech.* **2013**, *6* (11), 2989–3034. https://doi.org/10.5194/amt-6-2989-2013.

(3)   Hsu, N. C.; Lee, J.; Sayer, A. M.; Kim, W.; Bettenhausen, C.; Tsay, S. -C. VIIRS Deep Blue Aerosol Products Over Land: Extending the EOS Long-Term Aerosol Data Records. *J. Geophys. Res. Atmos.* **2019**, *124* (7), 4026–4053. https://doi.org/10.1029/2018JD029688.

(4)   Gupta, P.; Levy, R. C.; Mattoo, S.; Remer, L. A.; Munchak, L. A. A Surface Reflectance Scheme for Retrieving Aerosol Optical Depth over Urban Surfaces in MODIS Dark Target Retrieval Algorithm. *Atmos. Meas. Tech.* **2016**, *9* (7), 3293–3308. https://doi.org/10.5194/amt-9-3293-2016.

(5)   Sayer, A. M.; Hsu, N. C.; Lee, J.; Kim, W. V.; Dutcher, S. T. Validation, Stability, and Consistency of MODIS Collection 6.1 and VIIRS Version 1 Deep Blue Aerosol Data Over Land. *J. Geophys. Res. Atmos.* **2019**, *124* (8), 4658–4688. https://doi.org/10.1029/2018JD029598.

(6)   Lyapustin, A.; Wang, Y.; Korkin, S.; Huang, D. MODIS Collection 6 MAIAC Algorithm. *Atmos. Meas. Tech.* **2018**, *11* (10), 5741–5765. https://doi.org/10.5194/amt-11-5741-2018.

(7)   Lyapustin, A.; Wang, Y.; Xiong, X.; Meister, G.; Platnick, S.; Levy, R.; Franz, B.; Korkin, S.; Hilker, T.; Tucker, J.; et al. Scientific Impact of MODIS C5 Calibration Degradation and C6+ Improvements. *Atmos. Meas. Tech.* **2014**, *7* (12), 4353–4365. https://doi.org/10.5194/amt-7-4353-2014.

(8)   Sayer, A. M.; Hsu, N. C.; Bettenhausen, C.; Jeong, M.-J.; Holben, B. N.; Zhang, J. Global and Regional Evaluation of Over-Land Spectral Aerosol Optical Depth Retrievals from SeaWiFS. *Atmos. Meas. Tech.* **2012**, *5* (7), 1761–1778. https://doi.org/10.5194/amt-5-1761-2012.

(9)   Hsu, N. C.; Jeong, M.-J.; Bettenhausen, C.; Sayer, A. M.; Hansell, R.; Seftor, C. S.; Huang, J.; Tsay, S.-C. Enhanced Deep Blue Aerosol Retrieval Algorithm: The Second Generation. *J. Geophys. Res. Atmos.* **2013**, *118* (16), 9296–9315. https://doi.org/10.1002/jgrd.50712.

(10)   Diner, D. J.; Beckert, J. C.; Reilly, T. H.; Bruegge, C. J.; Conel, J. E.; Kahn, R. A.; Martonchik, J. V.; Ackerman, T. P.; Davies, R.; Gerstl, S. A. W.; et al. Multi-Angle Imaging SpectroRadiometer (MISR) Instrument Description and Experiment Overview. *IEEE Trans. Geosci. Remote Sens.* **1998**, *36* (4), 1072–1087. https://doi.org/10.1109/36.700992.

(11)   Martonchik, J. V.; Kahn, R. A.; Diner, D. J. Retrieval of Aerosol Properties over Land Using MISR Observations. In *Satellite Aerosol Remote Sensing over Land*; Springer

Berlin Heidelberg: Berlin, Heidelberg, 2009; pp 267–293. https://doi.org/10.1007/978-3-540-69397-0_9.

(12) Garay, M. J.; Witek, M. L.; Kahn, R. A.; Seidel, F. C.; Limbacher, J. A.; Bull, M. A.; Diner, D. J.; Hansen, E. G.; Kalashnikova, O. V.; Lee, H.; et al. Introducing the 4.4km Spatial Resolution Multi-Angle Imaging SpectroRadiometer (MISR) Aerosol Product. *Atmos. Meas. Tech.* **2020**, *13* (2), 593–628. https://doi.org/10.5194/amt-13-593-2020.

(13) Garay, M. J.; Kalashnikova, O. V.; Bull, M. A. Development and Assessment of a Higher-Spatial-Resolution (4.4 km) MISR Aerosol Optical Depth Product Using AERONET-DRAGON Data. *Atmos. Chem. Phys.* **2017**, *17* (8), 5095–5106. https://doi.org/10.5194/acp-17-5095-2017.

(14) Molod, A.; Takacs, L.; Suarez, M.; Bacmeister, J. Development of the GEOS-5 Atmospheric General Circulation Model: Evolution from MERRA to MERRA2. *Geosci. Model Dev.* **2015**, *8* (5), 1339–1356. https://doi.org/10.5194/gmd-8-1339-2015.

(15) Philip, S.; Martin, R. V.; Keller, C. A. Sensitivity of Chemistry-Transport Model Simulations to the Duration of Chemical and Transport Operators: A Case Study with GEOS-Chem V10-01. *Geosci. Model Dev.* **2016**, *9* (5), 1683–1695. https://doi.org/10.5194/gmd-9-1683-2016.

(16) Lin, J.-T.; McElroy, M. B. Impacts of Boundary Layer Mixing on Pollutant Vertical Profiles in the Lower Troposphere: Implications to Satellite Remote Sensing. *Atmos. Environ.* **2010**, *44* (14), 1726–1739. https://doi.org/10.1016/J.ATMOSENV.2010.02.009.

(17) Bey, I.; Jacob, D. J.; Yantosca, R. M.; Logan, J. A.; Field, B. D.; Fiore, A. M.; Li, Q.; Liu, H. Y.; Mickley, L. J.; Schultz, M. G. Global Modeling of Tropospheric Chemistry with Assimilated Meteorology: Model Description and Evaluation. *J. Geophys. Res.* **2001**, *106* (D19), 23073. https://doi.org/10.1029/2001JD000807.

(18) Park, R. J.; Jacob, D. J.; Field, B. D.; Yantosca, R. M.; Chin, M. Natural and Transboundary Pollution Influences on Sulfate-Nitrate-Ammonium Aerosols in the United States: Implications for Policy. *J. Geophys. Res.* **2004**, *109* (D15), D15204. https://doi.org/10.1029/2003JD004473.

(19) Fountoukis, C.; Nenes, A. ISORROPIA II: A Computationally Efficient Thermodynamic Equilibrium Model for K^+–Ca^{2+}–Mg^{2+}–NH_4^+–Na^+–SO_4^{2-}–NO_3^-–Cl^-–H_2O Aero. *Atmos. Chem. Phys.* **2007**, *7* (17), 4639–4659. https://doi.org/10.5194/acp-7-4639-2007.

(20) Pye, H. O. T.; Liao, H.; Wu, S.; Mickley, L. J.; Jacob, D. J.; Henze, D. K.; Seinfeld, J. H. Effect of Changes in Climate and Emissions on Future Sulfate-Nitrate-Ammonium Aerosol Levels in the United States. *J. Geophys. Res. Atmos.* **2009**, *114* (D1). https://doi.org/10.1029/2008JD010701.

(21) Park, R. J.; Jacob, D. J.; Chin, M.; Martin, R. V. Sources of Carbonaceous Aerosols over the United States and Implications for Natural Visibility. *J. Geophys. Res.* **2003**, *108* (D12), 4355. https://doi.org/10.1029/2002JD003190.

(22) Jaeglé, L.; Quinn, P. K.; Bates, T. S.; Alexander, B.; Lin, J.-T. Global Distribution of Sea Salt Aerosols: New Constraints from in Situ and Remote Sensing Observations. *Atmos. Chem. Phys.* **2011**, *11* (7), 3137–3157. https://doi.org/10.5194/acp-11-3137-2011.

(23) Fairlie, D. J.; Jacob, D. J.; Park, R. J. The Impact of Transpacific Transport of Mineral Dust in the United States. *Atmos. Environ.* **2007**, *41* (6), 1251–1266. https://doi.org/10.1016/j.atmosenv.2006.09.048.

(24) Zhang, L.; Kok, J. F.; Henze, D. K.; Li, Q.; Zhao, C. Improving Simulations of Fine Dust Surface Concentrations over the Western United States by Optimizing the Particle Size Distribution. *Geophys. Res. Lett.* **2013**, *40* (12), 3270–3275. https://doi.org/10.1002/grl.50591.

(25) Philip, S.; Martin, R. V; Snider, G.; Weagle, C. L.; van Donkelaar, A.; Brauer, M.; Henze, D. K.; Klimont, Z.; Venkataraman, C.; Guttikunda, S. K.; et al. Anthropogenic Fugitive, Combustion and Industrial Dust Is a Significant, Underrepresented Fine Particulate Matter Source in Global Atmospheric Models. *Environ. Res. Lett.* **2017**, *12* (4), 044018. https://doi.org/10.1088/1748-9326/aa65a4.

(26) Pye, H. O. T.; Chan, A. W. H.; Barkley, M. P.; Seinfeld, J. H. Global Modeling of Organic Aerosol: The Importance of Reactive Nitrogen (NO<Sub>X</Sub> and NO<Sub>3</Sub>). *Atmos. Chem. Phys.* **2010**, *10* (22), 11261–11276. https://doi.org/10.5194/acp-10-11261-2010.

(27) Marais, E. A.; Jacob, D. J.; Jimenez, J. L.; Campuzano-Jost, P.; Day, D. A.; Hu, W.; Krechmer, J.; Zhu, L.; Kim, P. S.; Miller, C. C.; et al. Aqueous-Phase Mechanism for Secondary Organic Aerosol Formation from Isoprene: Application to the Southeast United States and Co-Benefit of SO<Sub>2</Sub> Emission Controls. *Atmos. Chem. Phys.* **2016**, *16* (3), 1603–1618. https://doi.org/10.5194/acp-16-1603-2016.

(28) Heald, C. L.; J. L. Collett Jr., J. L.; Lee, T.; Benedict, K. B.; Schwandner, F. M.; Li, Y.; Clarisse, L.; Hurtmans, D. R.; Van Damme, M.; Clerbaux, C.; et al. Atmospheric Ammonia and Particulate Inorganic Nitrogen over the United States. *Atmos. Chem. Phys.* **2012**, *12* (21), 10295–10312. https://doi.org/10.5194/acp-12-10295-2012.

(29) Koepke, P.; Hess, M.; Schult, I.; Shettle, E. P. *Global Aerosol Dataset*; report, Max-Planck Inst. fur Meteorol., Hamburg, Germany, 1997.

(30) Martin, R. V.; Jacob, D. J.; Yantosca, R. M.; Chin, M.; Ginoux, P. Global and Regional Decreases in Tropospheric Oxidants from Photochemical Effects of Aerosols. *J. Geophys. Res.* **2003**, *108* (D3), 4097. https://doi.org/10.1029/2002JD002622.

(31) Drury, E.; Jacob, D. J.; Spurr, R. J. D.; Wang, J.; Shinozuka, Y.; Anderson, B. E.; Clarke, A. D.; Dibb, J.; McNaughton, C.; Weber, R. Synthesis of Satellite (MODIS), Aircraft (ICARTT), and Surface (IMPROVE, EPA-AQS, AERONET) Aerosol Observations over Eastern North America to Improve MODIS Aerosol Retrievals and Constrain Surface Aerosol Concentrations and Sources. *J. Geophys. Res.* **2010**, *115* (D14), D14204. https://doi.org/10.1029/2009JD012629.

(32) Lee, C.; Martin, R. V.; van Donkelaar, A.; O'Byrne, G.; Krotkov, N.; Richter, A.; Huey, L. G.; Holloway, J. S. Retrieval of Vertical Columns of Sulfur Dioxide from SCIAMACHY and OMI: Air Mass Factor Algorithm Development, Validation, and Error Analysis. *J. Geophys. Res.* **2009**, *114* (D22), D22303. https://doi.org/10.1029/2009JD012123.

(33) Ridley, D. A.; Heald, C. L.; Ford, B. North African Dust Export and Deposition: A

Satellite and Model Perspective. *J. Geophys. Res.* **2012**, *117* (D2), D02202. https://doi.org/10.1029/2011JD016794.

(34)   Hammer, M. S.; Martin, R. V.; van Donkelaar, A.; Buchard, V.; Torres, O.; Ridley, D. A.; Spurr, R. J. D. Interpreting the Ultraviolet Aerosol Index Observed with the OMI Satellite Instrument to Understand Absorption by Organic Aerosols: Implications for Atmospheric Oxidation and Direct Radiative Effects. *Atmos. Chem. Phys.* **2016**, *16* (4), 2507–2523. https://doi.org/10.5194/acp-16-2507-2016.

(35)   Crippa, M.; Janssens-Maenhout, G.; Dentener, F.; Guizzardi, D.; Sindelarova, K.; Muntean, M.; Van Dingenen, R.; Granier, C. Forty Years of Improvements in European Air Quality: Regional Policy-Industry Interactions with Global Impacts. *Atmos. Chem. Phys.* **2016**, *16* (6), 3825–3841. https://doi.org/10.5194/acp-16-3825-2016.

(36)   Schultz, M.; Rast, S.; for Meteorology, M.; Authors, H.; van het Bolscher, M.; Pulles, T.; Brand, R.; Jose Pereira, A.; Mota, B.; Allan Spessa, L.; et al. *REanalysis of the TROpospheric Chemical Composition over the Past 40 Years A Long-Term Global Modeling Study of Tropospheric Chemistry Funded under the 5 Th EU Framework Programme EU-Contract N o Emission Data Sets and Methodologies for Estimating Emissions Work Package 1, Deliverable D1-6 Editor: (Modified Annex 4) RETRO Deliverable D1-6: Report on Emissions / 2 RETRO Deliverable D1-6: Report on Emissions / 3*.

(37)   Travis, K. R.; Jacob, D. J.; Fisher, J. A.; Kim, P. S.; Marais, E. A.; Zhu, L.; Yu, K.; Miller, C. C.; Yantosca, R. M.; Sulprizio, M. P.; et al. Why Do Models Overestimate Surface Ozone in the Southeast United States? *Atmos. Chem. Phys.* **2016**, *16* (21), 13561–13577. https://doi.org/10.5194/acp-16-13561-2016.

(38)   Kuhns, H.; Knipping, E. M.; Vukovich, J. M. Development of a United States–Mexico Emissions Inventory for the Big Bend Regional Aerosol and Visibility Observational (BRAVO) Study. *J. Air Waste Manage. Assoc.* **2005**, *55* (5), 677–692. https://doi.org/10.1080/10473289.2005.10464648.

(39)   Li, M.; Zhang, Q.; Kurokawa, J.; Woo, J.-H.; He, K.; Lu, Z.; Ohara, T.; Song, Y.; Streets, D. G.; Carmichael, G. R.; et al. MIX: A Mosaic Asian Anthropogenic Emission Inventory under the International Collaboration Framework of the MICS-Asia and HTAP. *Atmos. Chem. Phys.* **2017**, *17* (2), 935–963. https://doi.org/10.5194/acp-17-935-2017.

(40)   Liu, F.; Zhang, Q.; van der A, R. J.; Zheng, B.; Tong, D.; Yan, L.; Zheng, Y.; He, K. Recent Reduction in NO$_x$ Emissions over China: Synthesis of Satellite Observations and Emission Inventories. *Environ. Res. Lett.* **2016**, *11* (11), 114002. https://doi.org/10.1088/1748-9326/11/11/114002.

(41)   Lu, Z.; Zhang, Q.; Streets, D. G. Sulfur Dioxide and Primary Carbonaceous Aerosol Emissions in China and India. *Atmos. Chem. Phys. Atmos. Chem. Phys.* **2011**, *11*, 9839–9864. https://doi.org/10.5194/acp-11-9839-2011.

(42)   Philip, S.; Martin, R. V.; van Donkelaar, A.; Lo, J. W.-H.; Wang, Y.; Chen, D.; Zhang, L.; Kasibhatla, P. S.; Wang, S.; Zhang, Q.; et al. Global Chemical Composition of Ambient Fine Particulate Matter for Exposure Assessment. *Environ. Sci. Technol.* **2014**, *48* (22), 13060–13068. https://doi.org/10.1021/es502965b.

(43) Fu, T.-M.; Cao, J. J.; Zhang, X. Y.; Lee, S. C.; Zhang, Q.; Han, Y. M.; Qu, W. J.; Han, Z.; Zhang, R.; Wang, Y. X.; et al. Carbonaceous Aerosols in China: Top-down Constraints on Primary Sources and Estimation of Secondary Contribution. *Atmos. Chem. Phys.* **2012**, *12* (5), 2725–2746. https://doi.org/10.5194/acp-12-2725-2012.

(44) Giglio, L.; Randerson, J. T.; van der Werf, G. R. Analysis of Daily, Monthly, and Annual Burned Area Using the Fourth-Generation Global Fire Emissions Database (GFED4). *J. Geophys. Res. Biogeosciences* **2013**, *118* (1), 317–328. https://doi.org/10.1002/jgrg.20042.

(45) van Donkelaar, A.; Martin, R. V.; Brauer, M.; Hsu, N. C.; Kahn, R. A.; Levy, R. C.; Lyapustin, A.; Sayer, A. M.; Winker, D. M. Global Estimates of Fine Particulate Matter Using a Combined Geophysical-Statistical Method with Information from Satellites, Models, and Monitors. *Environ. Sci. Technol.* **2016**, *50* (7), 3762–3772. https://doi.org/10.1021/acs.est.5b05833.

(46) Holben, B. N.; Eck, T. F.; Slutsker, I.; Tanré, D.; Buis, J. P.; Setzer, A.; Vermote, E.; Reagan, J. A.; Kaufman, Y. J.; Nakajima, T.; et al. AERONET—A Federated Instrument Network and Data Archive for Aerosol Characterization. *Remote Sens. Environ.* **1998**, *66* (1), 1–16. https://doi.org/10.1016/S0034-4257(98)00031-5.

(47) Giles, D. M.; Sinyuk, A.; Sorokin, M. G.; Schafer, J. S.; Smirnov, A.; Slutsker, I.; Eck, T. F.; Holben, B. N.; Lewis, J. R.; Campbell, J. R.; et al. Advancements in the Aerosol Robotic Network (AERONET) Version 3 Database – Automated near-Real-Time Quality Control Algorithm with Improved Cloud Screening for Sun Photometer Aerosol Optical Depth (AOD) Measurements. *Atmos. Meas. Tech.* **2019**, *12* (1), 169–209. https://doi.org/10.5194/amt-12-169-2019.

(48) Li, Z.; Zhao, X.; Kahn, R.; Mishchenko, M.; Remer, L.; Lee, K.-H.; Wang, M.; Laszlo, I.; Nakajima, T.; Maring, H. Uncertainties in Satellite Remote Sensing of Aerosols and Impact on Monitoring Its Long-Term Trend: A Review and Perspective. *Ann. Geophys.* **2009**, *27* (7), 2755–2770. https://doi.org/10.5194/angeo-27-2755-2009.

(49) Friedl, M. A.; Sulla-Menashe, D.; Tan, B.; Schneider, A.; Ramankutty, N.; Sibley, A.; Huang, X. MODIS Collection 5 Global Land Cover: Algorithm Refinements and Characterization of New Datasets. *Remote Sens. Environ.* **2010**, *114* (1), 168–182. https://doi.org/10.1016/J.RSE.2009.08.016.

(50) van Donkelaar, A.; Martin, R. V.; Spurr, R. J. D.; Drury, E.; Remer, L. A.; Levy, R. C.; Wang, J. Optimal Estimation for Global Ground-Level Fine Particulate Matter Concentrations. *J. Geophys. Res. Atmos.* **2013**, *118* (11), 5621–5636. https://doi.org/10.1002/jgrd.50479.

(51) Brunsdon, C.; Fotheringham, A. S.; Charlton, M. E. Geographically Weighted Regression: A Method for Exploring Spatial Nonstationarity. *Geogr. Anal.* **2010**, *28* (4), 281–298. https://doi.org/10.1111/j.1538-4632.1996.tb00936.x.

(52) Shaddick, G.; Thomas, M. L.; Green, A.; Brauer, M.; van Donkelaar, A.; Burnett, R.; Chang, H. H.; Cohen, A.; Dingenen, R. Van; Dora, C.; et al. Data Integration Model for Air Quality: A Hierarchical Approach to the Global Estimation of Exposures to Ambient Air Pollution. *J. R. Stat. Soc. Ser. C (Applied Stat.* **2018**, *67* (1), 231–253. https://doi.org/10.1111/rssc.12227.

(53)   CIESIN (Center for International Earth Science Information Network). Gridded
         Population of the World Version 4. NASA Socioeconomic Data and Applications Center
         (SEDAC): Palisades, NY 2017, pp 1–21. https://doi.org/10.1128/AAC.03728-14.